

# Active suppression of finite-amplitude Rayleigh–Bénard convection

By A. C. OR AND J. L. SPEYER

Department of Mechanical and Aerospace Engineering, University of California, Los Angeles,  
CA 90095-1597, USA

(Received 29 May 2002 and in revised form 26 December 2002)

We study by a fully nonlinear three-dimensional pseudospectral time-splitting simulation, the feedback control of a layer of fluid heated from below. The initial condition corresponds to a steady large-amplitude preferred convection state obtained at Prandtl number of 7.0 and Rayleigh number of  $10^4$ , which is about six times the Rayleigh critical value. A robust controller based on the LQG (linear–quadratic–Gaussian) synthesis method is used. Both sensors and actuator are thermal-based, planar, and assumed to be continuously distributed. The simulated results show that large-amplitude steady-state convection rolls can be suppressed by the linear LQG controller action. The Green's function of the controller gives the shape of the control action corresponding to a point measurement. In addition, for Rayleigh numbers below the proportional feedback control stability limit, this controller appeared to be effective in damping out steady-state convection rolls as well. However, in a region very near the proportional control stability limit, proportional control action induces subcritical g-type hexagonal convection, which is obtained here through direct simulations. Note that well above this proportional control limit, the LQG still damps out all convection. The nonlinear plant model is validated by comparing check cases with published results.

---

## 1. Introduction

Active suppression of onset of convection in a layer of fluid has potentially important applications in improving the material that goes through solidification in a mould. For instance, during the growth phase of large silicon wafers or composite materials, a large thermal gradient typically causes undesirable convective motions in the melt. To understand the active control of the realistic manufacturing process, an idealized system is an important starting point. To this end Rayleigh–Bénard convection (RBC) is ideal for vigorous theoretical analysis.

Many theoretical studies have employed the linear feedback control to increase the stability threshold of the purely heat conductive state so that no convection occurs despite the presence of a large thermal gradient (Tang & Bau 1993, 1994, 1998*a, b*; Howle 1997*a, b, c*, 2000; Or, Cortelezzi & Speyer 2001). These studies used the linear plant model and employed a simple controller using the proportional feedback. The implantable sensor and actuator are assumed to be of the thermal type and continuously distributed spatially on the horizontal plane. Analysis as well as experimental results in general indicate that the proportional controller will stabilize the basic state up to Rayleigh number ( $Ra$ ) of 3 to 4 times its critical value of the basic state (see Tang & Bau 1994; Howle 1997*a*). Furthermore, as shown in

Tang & Bau (1994), a controller-induced oscillatory instability occurs at a large gain. A linear–quadratic–Gaussian (LQG) controller has also been studied (Or *et al.* 2001) to increase the region of stabilization and with a higher margin of robustness. First, the stability limit can be raised to about 14 times the critical value of  $Ra$ . Secondly, the gain and phase margins about the design point of the controller appear adequate for practical implementation.

To develop a control design to be implementable for applicational processes (such as for crystal growth or a melt), it is crucial to understand the control process for simpler geometry and material properties. We have been focused on an Oberbeck–Boussinesq model for a horizontal layer of fluid. The plant dynamics is known as Rayleigh–Bénard convection (RBC) (Cross & Hohenberg 1993). As a first step, the performance of the linear controller design for the linear plant dynamics is reported in Or *et al.* (2001). In this paper, as a step further, the focus is turned to the performance of the linear controller design for the fully nonlinear plant dynamics.

It is well known that in a large layer of heated fluid, convection occurs as a steady pattern of two-dimensional rolls. The two-dimensional convection rolls and the stability properties were investigated in detail by Clever & Busse (1974) and Busse & Clever (1979). For the heated layer corresponding to  $Ra > Ra_{c0}$  ( $Ra_{c0}$  is computed theoretically to have the value of 1707.762 up to 3 decimal places), the stable roll pattern occurs only within a band of wavenumber centred approximately about the critical wavenumber  $\alpha_c = 3.117$ . Within the stable band the rolls realized do not necessarily have a preferred length scale. Indeed, their wavelength appears to be dictated by the initial conditions used to select the rolls and by the manner that the basic state temperature is prescribed spatially and temporally. The band is bounded on both sides by instabilities that pertain to changing the wavelength of the rolls but not changing the planform. As the induced rolls acquire a wavelength too large or too small, an instability will occur to shift their length scale back to a value close to the critical value. As the value of  $Ra$  increases, the rolls will at some point become unstable and the convection structure will converge to a pattern with more complex spatial or temporal structure. The exact value of  $Ra$  at which the transition occurs is wavenumber dependent. For a Prandtl number ( $Pr$ ) of 7.0, for instance, the two-dimensional rolls become unstable to a three-dimensional bimodal convection at roughly  $Ra \approx 25Ra_{c0}$  at the wavenumber of about 2.0 (see the experimental observations presented in figure 11, Busse & Clever 1979). The transition highlights a sufficiently strong thermal boundary-layer effect, made possible at  $Ra$  values. The transition to three-dimensional convection occurs at a significantly higher  $Ra$  threshold than the closed-loop stability limit of  $14.5Ra_{c0}$  based on the linear LQG controller (Or *et al.* 2001). For our control analysis here, therefore, we need only to consider the two-dimensional rolls as the initial state of convection to be controlled.

Our present control problem can be investigated most effectively by the use of time-domain analysis. A three-dimensional fully nonlinear pseudospectral model using a time-splitting integration method is developed, based on the Oberbeck–Boussinesq equations. The proportional feedback controller is easily implementable. This case provides the check cases for code validation purposes. Certain flow patterns that are known to be induced by the controller effects, such as the oscillation mode (Tang & Bau 1994) and the g-type hexagons (Or & Kelly 2001), can be obtained here from the direct numerical simulations and compared with those reported from previous analyses. In §2, the nonlinear plant model and the LQG controller will be briefly described. The results will be presented in §3, followed by the conclusion in §4.

## 2. Mathematical formulation

### 2.1. Nonlinear plant model and numerical solution

The nonlinear plant model is governed by the Oberbeck–Boussinesq equations for a horizontal layer of fluid. In the non-dimensional form  $d$ ,  $d^2/\kappa$ ,  $\kappa/d$ ,  $\kappa/d^2$ ,  $\rho(\kappa/d)^2$  and  $\Delta T$  are used as the scales of length, time, velocity, vorticity, pressure and temperature, where  $d$  is the layer thickness,  $\kappa$  and  $\rho$  are the mean thermal diffusivity and density of the fluid, and  $\Delta T$  is the temperature difference between the upper and lower wall in the purely conductive basic state. The governing non-dimensional equations are,

$$Pr^{-1} \partial_t \mathbf{v} = Pr^{-1} \mathbf{v} \times \boldsymbol{\omega} + \mathbf{k} Ra \theta - \nabla \pi + \nabla^2 \mathbf{v}, \quad (2.1)$$

$$\partial_t \theta = -\mathbf{v} \cdot \nabla \theta + w + \nabla^2 \theta, \quad (2.2)$$

$$\nabla \cdot \mathbf{v} = 0, \quad (2.3)$$

where  $\mathbf{v} = (u, v, w)$  is the velocity vector field,  $\boldsymbol{\omega} = \nabla \times \mathbf{v}$  is the vorticity,  $\pi = p + \mathbf{v} \cdot \mathbf{v}/2$  is the pressure head,  $\theta$  is the perturbation temperature and  $\mathbf{k}$  is the unit vector in the  $z$ -direction. The two external parameters are Rayleigh and Prandtl numbers, given by  $Ra = g \Delta T d^3 / \nu \kappa$  and  $Pr = \nu / \kappa$  where  $\nu$  is the mean kinematic viscosity. The continuity equation (2.3) applies only when the flow is incompressible.

The velocity field is assumed to be non-permeable and non-slip at the upper and lower walls, thus subject to

$$\mathbf{v}(x, y, 0, t) = \mathbf{0}, \quad \mathbf{v}(x, y, 1, t) = \mathbf{0}. \quad (2.4)$$

The temperature field, on the other hand, is assumed to satisfy the isothermal condition at the upper wall. The lower wall is non-isothermal owing to the action of the thermal actuation. It is assumed that a control temperature  $\theta_c(x, y, t)$  can be imposed. The upper and lower thermal boundary conditions for the perturbation field are therefore

$$\theta(x, y, 1, t) = 0, \quad \theta(x, y, 0, t) = \theta_c(x, y, t). \quad (2.5)$$

In order to perform the feedback control, the perturbation temperature field has to be measured in the fluid. In our model, three sensor planes are embedded in the layer at carefully chosen levels at  $z = z_s$  (with  $s = 1, 2$  and  $3$ ). For analysis purposes, these sensor planes are assumed to exert no blockage effects on the flow field. They measure the planar temperature distribution in the layer,

$$\theta(x, y, z_s, t) = \theta_s(x, y, t), \quad s = 1, 2, 3. \quad (2.6)$$

Assuming a continuous-distributed sensor,  $\theta_s(x, y, t)$  are known at sampled points and time.

In the numerical scheme, the dependent variables  $u$ ,  $v$ ,  $w$ ,  $p$  and  $\theta$  are expressed by the following truncated, triple sums,

$$\begin{bmatrix} u \\ v \\ w \\ p \\ \theta \end{bmatrix} (x, y, z, t) = \text{Re} \left\{ \sum_{n=0}^N \sum_{k=0}^K \sum_{m=-M+1}^M \begin{bmatrix} u_{kmn} \\ v_{kmn} \\ w_{kmn} \\ p_{kmn} \\ \theta_{kmn} \end{bmatrix} (t) T_n(z) \exp(i(k\alpha_x x + m\alpha_y y)) \right\} \quad (2.7)$$

where  $\text{Re}$  denotes the real part of the sum,  $\alpha_x$  and  $\alpha_y$  are the fundamental wavenumbers in the  $x$ - and  $y$ -directions, respectively. The asymmetric treatment of the indices  $k$  and  $m$  reduces the number of coefficients by half because the velocity, pressure and temperature are real dependent variables (see Marcus 1984). These two parameters are prescribed in the model. The functions  $T_n(z)$  ( $n = 0, 1, \dots$ ) denote the

Chebyshev polynomials. Note that a linear coordinate transformation is implicitly assumed to convert the Chebyshev function domain between  $+1$  and  $-1$  to our physical range  $0 \leq z < 1$ . The actuator and sensor temperatures,  $\theta_c$  and  $\theta_s$  ( $s = 1, 2$  and  $3$ ), are planar (two-dimensional). They are expanded in double series in a similar fashion,

$$\begin{bmatrix} \theta_s(z_1, t) \\ \theta_s(z_2, t) \\ \theta_s(z_3, t) \\ \theta_c(0, t) \end{bmatrix} (x, y, t) = \text{Re} \left\{ \sum_{k=0}^K \sum_{m=-M+1}^M \begin{bmatrix} \theta_{km,s}(z_1, t) \\ \theta_{km,s}(z_2, t) \\ \theta_{km,s}(z_3, t) \\ \theta_{km,c}(0, t) \end{bmatrix} \exp(i(k\alpha_x x + m\alpha_y y)) \right\}. \quad (2.8)$$

In our terminology, the lower thermal boundary condition (2.5) and the sensor equations (2.6) are, respectively, the input to and output from the nonlinear plant model.

The nonlinear equations, together with the boundary and the continuity equations are then solved numerically by using the pseudospectral, time-splitting integration technique (Gottlieb & Orszag 1977; Canuto *et al.* 1986; Bodenschatz, Pesch & Ahlers 2000). Marcus (1984) provided a detailed description of the implementation of the method for the Taylor-vortex flow simulations. Using the time-splitting method, an integration time step is split into three fractional steps. The first is a nonlinear fractional step, typically done using an explicit, second-order Adams–Bashforth scheme,

$$\mathbf{v}^{N+1/3} = \mathbf{v}^N + \Delta t \frac{3}{2} [\mathbf{v}^N \times \boldsymbol{\omega}^N + PrRa\theta^N \mathbf{k}] - \Delta t \frac{1}{2} [\mathbf{v}^{N-1} \times \boldsymbol{\omega}^{N-1} + PrRa\theta^{N-1} \mathbf{k}], \quad (2.9)$$

$$\theta^{N+1/3} = \theta^N - \Delta t \frac{3}{2} [\mathbf{v}^N \cdot \nabla \theta^N - w^N] + \Delta t \frac{1}{2} [\mathbf{v}^{N-1} \cdot \nabla \theta^{N-1} - w^{N-1}]. \quad (2.10)$$

The superscript  $N$  here denotes the time step and is not to be confused with the truncation number for the vertical dependence. A significant fraction of the total computation load occurs in computing the nonlinear terms. In the collocation space, the nonlinear terms are computed spatially by point-by-point multiplications. However, fast Fourier transforms (FFT) and inverse fast Fourier transforms (IFFT) have to be used to convert the field back and forth between the collocation and the Chebyshev–Fourier spaces. The fast Fourier transform (FFT) and inverse fast Fourier transform (IFFT) routines are obtained from the library of the *Numerical Recipes* (Press *et al.* 1992), with some minor modifications. For validation, these routines have been checked against the standard *Matlab* FFT and IFFT functions and match up to 15 decimal places. For typical flow fields, the truncation errors from FFT and IFFT due to aliasing are mainly small (Marcus 1984; Press *et al.* 1992). We note that, however, that the FFT method can still be computationally demanding for high-resolution solutions. The pseudospectral method is generally known to be efficient. There also exist other efficient methods not using the transforms, for instance, the reduced-order Galerkin method (Howle 1996).

After obtaining the  $(N + 1/3)$ th fractional step with the Adams–Bashforth scheme, we compute the  $(N + 1)$ th step from the following equation,

$$(1 - Pr\Delta t \nabla^2) \mathbf{v}^{N+1} = \mathbf{v}^{N+1/3} - Pr\Delta t \nabla \pi, \quad (2.11)$$

subject to  $\nabla \cdot \mathbf{v}^{N+1} = 0$ . It is noted that, in general,  $\nabla \cdot \mathbf{v}^{N+1/3} \neq 0$ . The most straightforward procedure for solving (2.11) appears to be splitting the equation into a pressure step and a viscous step (we refer to it as the direct approach). In the pressure step, the flow field subject to a no normal-flow boundary condition at the walls can be solved from a Poisson equation, based on the property that the

pressure field is irrotational and the flow field satisfies the continuity constraint (2.3). Next, a diffusive fractional step completes the solution of the fractional velocity and temperature fields by prescribing the no-slip and thermal boundary conditions at the walls. As simple as it appeared, the scheme had problems computing the correct flow field. In his numerical simulation of Taylor vortex flow, Marcus (1984) reported large boundary errors using this direct approach. In his discussions it was argued that the shear may play a role and it is not clear whether a similar problem will occur for RBC. In our study we have applied the direct scheme in our preliminary simulations and observed large errors even for the open-loop simulations. Thus, it appears that the problem is common to both Taylor vortex flows and RBC. For more detail about the cause of the large boundary errors in the direct approach, we refer to Marcus (1984). Marcus identified the source of errors and developed a procedure to correct it. His remedy is to further split the fractional solution into a complementary and a particular solution so that the boundary conditions and the continuity equations are satisfied numerically. The procedure, however, involves the additional computation of several Green’s functions and seems elaborate. Since the boundary-value problem corresponding to (2.11) is linear, we anticipate there are simpler alternative approaches to resolve the numerical difficulty. Here, we solve the problem involving the pressure and viscous forces as a single step, without splitting the pressure and viscous terms. First, we use the continuity equation as the constraint and eliminate the two horizontal velocity components in favour of the vertical component. Secondly, we obtain the solution of the boundary-value problem for  $w$  and  $\theta$ . Finally, we recover  $u$  and  $v$  from  $w$ , Fourier mode by Fourier mode, again using the continuity equation. This scheme seems significantly simpler and has been tested here to be effective. Because of the simplicity, it is worth the description as an alternative approach to the time-splitting procedure.

By eliminating pressure from (2.11), we obtain a single scalar equation governing  $w$ ,

$$(1 - Pr\Delta t\nabla^2)\nabla^2\partial_z w^{N+1} = \nabla_{\perp}^2\partial_z w^{N+1/3} - \partial_{zz}^2(\partial_x u^{N+1/3} + \partial_y v^{N+1/3}). \quad (2.12)$$

The equation above is integrated in  $z$ , this gives

$$(1 - Pr\Delta t\nabla^2)\nabla^2 w^{N+1} = \nabla_{\perp}^2 w^{N+1/3} - (\partial_{xz}^2 u^{N+1/3} + \partial_{yz}^2 v^{N+1/3}). \quad (2.13)$$

The integration constant is zero because of the non-slip boundary condition. (This constant will depend on the initial conditions when the case of free-slip boundary conditions is considered). Equation (2.13) is of fourth-order spatially. It has to satisfy four boundary conditions, as follows,

$$w^{N+1} = 0, \quad \partial_z w^{N+1} = 0 \quad \text{at } z = 0, 1. \quad (2.14)$$

The fourth-order boundary-value problem, (2.12), determines  $w^{N+1}$ . After we have obtained  $w^{N+1}$ , the horizontal velocity components corresponding to  $w^{N+1}$  can be obtained by inverting the continuity and Helmholtz equations, Fourier mode by Fourier mode. In the expansion,  $w^{N+1}$  is given by

$$w^{N+1}(x, y, z, t) = \text{Re} \left\{ \sum_{k=0}^K \sum_{m=-M+1}^M w_{km}^{N+1}(z, t) \exp(i(k\alpha_x x + m\alpha_y y)) \right\}. \quad (2.15)$$

Similarly, the horizontal velocity components are

$$\begin{bmatrix} u^{N+1}(x, y, z, t) \\ v^{N+1}(x, y, z, t) \end{bmatrix} = \text{Re} \left\{ \sum_{k=0}^K \sum_{m=-M+1}^M \begin{bmatrix} u_{km}^{N+1}(z, t) \\ v_{km}^{N+1}(z, t) \end{bmatrix} \exp(i(k\alpha_x x + m\alpha_y y)) \right\}. \quad (2.16)$$

Each pair of coefficients  $(u_{km}^{N+1}, v_{km}^{N+1})$  now satisfies a Helmholtz equation

$$\nabla_{\perp}^2 \begin{bmatrix} u_{km}^{N+1} \\ v_{km}^{N+1} \end{bmatrix} = \alpha_{km}^2 \begin{bmatrix} u_{km}^{N+1} \\ v_{km}^{N+1} \end{bmatrix}, \quad (2.17)$$

where  $\alpha_{km} = \{(k\alpha_x)^2 + (m\alpha_y)^2\}^{1/2}$ . The Helmholtz equation together with the continuity equation allows us to solve for  $v_{km}^{N+1}$  in terms of  $w_{km}^{N+1}$ , provided that  $\alpha_{km} \neq 0$ . The condition  $\alpha_{km} \neq 0$  can occur in the case of a free-slip wall, but not in the case of a no-slip wall. We refer to the discussion of Cross & Hohenberg (1993, p. 970). The perturbation temperature field, on the other hand, is not constrained to have zero mean field. Using the continuity equation, we obtain the horizontal velocity components,

$$u_{km}^{N+1} = \frac{1}{\alpha_{km}^2} \partial_{xz}^2 w_{km}^{N+1}, \quad v_{km}^{N+1} = \frac{1}{\alpha_{km}^2} \partial_{yz}^2 w_{km}^{N+1}. \quad (2.18)$$

### 2.2. The proportional feedback controller

In the proportional feedback control, a proportional relationship is constructed between the input and output of the plant. As in the cases studied by Tang & Bau (1994) and Or *et al.* (2001), only one sensor plane is used and the control law in this case is

$$\theta_c(0, t) = -K_p \theta_s(z_s, t), \quad (2.19)$$

where  $K_p$  is a constant gain and  $z_s$  is the vertical height of the sensor plane. The controller is very simple for this case.

### 2.3. The LQG controller

The theory and design of the LQG controller was described in Or *et al.* (2001). In brief, the linear stability equations of the Fourier-decomposed system of convection and the measurement equation are given in matrix form, respectively, by

$$\dot{\mathbf{x}} = \mathbf{A}\mathbf{x} + \mathbf{B}\mathbf{u}, \quad \mathbf{z} = \mathbf{C}\mathbf{x}, \quad (2.20)$$

where the entries of the state vector  $\mathbf{x}$  are the Chebyshev coefficients of velocity and temperature perturbations;  $u$  (measured at plane  $z = 0$ ) and  $\mathbf{z}$  (measured at planes  $z_1, z_2$  and  $z_3$ ) are, respectively, the Fourier coefficients of the planar control and measured temperatures. Note that the Fourier-decomposed equations correspond to wavenumber  $\alpha_{km}$  and Rayleigh number  $Ra$ . The following modifications to the original formulation of the controller model (Or *et al.* 2001) have been made here: (i) the vertical dependence is expanded in terms of the Chebyshev polynomials instead of the beam functions as the basis functions. The expansion procedure, originally based on the Galerkin method, has been converted to the tau method. In the improved numerical procedure, we obtain the exact condition  $\mathbf{D} \equiv \mathbf{0}$ , in contrast to the previous condition that  $\mathbf{D} \rightarrow \mathbf{0}$  only as  $N \rightarrow \infty$ . (ii) We no longer consider the wavenumber as a prescribed parameter here. Instead, an individual modal controller is developed for each set of wavenumbers  $(k\alpha_x, m\alpha_y)$ . There is a set of state-space equations for each wave vector. In total, there are  $2(K+1)M$  sets of  $\mathbf{A}$ ,  $\mathbf{B}$  and  $\mathbf{C}$  matrices to be processed.

The LQG controller is comprised of a Kalman filter and an optimal regulator. The Kalman filter equation and the optimal regulator equation corresponding to the state-space equations, (2.20), are, respectively,

$$\dot{\hat{\mathbf{x}}} = \mathbf{A}^* \hat{\mathbf{x}} + \mathbf{B}^* \mathbf{u} + \mathbf{K}_f (z - \hat{z}), \quad \dot{\hat{z}} = \mathbf{C}^* \hat{\mathbf{x}}, \quad u = -\mathbf{K}_c \hat{\mathbf{x}}, \quad (2.21)$$

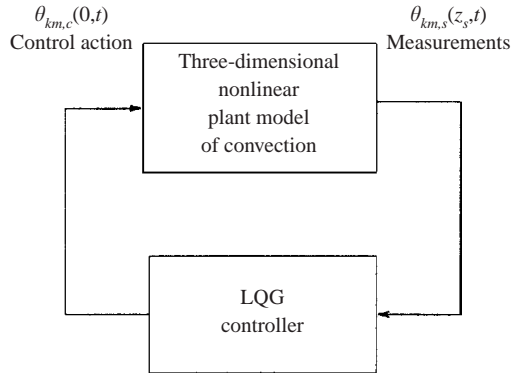


FIGURE 1. The LQG control loop diagram.

where  $\mathbf{x}$  is the estimate state vector. We distinguish the matrices with asterisk superscripts to highlight that the system is computed at a nominal (designed) wavenumber and Rayleigh number,  $(\alpha_{km}^*, Ra^*)$ . The Kalman gain vector  $\mathbf{K}_f$  and the optimal gain vector  $\mathbf{K}_c$  are determined from separate steady-state algebraic Riccati equations. The Kalman filter is used here as a state observer rather than as an estimator since no noises are injected into the system simulation. The cost functional, weighting and filter parameters chosen for controller design are described in detail in Or *et al.* (2001) which will not be repeated here. For robustness, in the design, the Kalman filter input matrix  $\mathbf{G}$  has been set equal to the control input matrix  $\mathbf{B}$ , a step known as the loop transfer recovery to recover the full-state feedback performance of the optimal regulator. The weights for the objective functions, as well as the filter parameters and the loop transfer recovery are described in Or *et al.* (2001).

It is worth noting that the LQG controller is a variant of the  $H_\infty$  controller when the disturbance attenuation bound is infinite (see Rhee & Speyer 1991). In Or *et al.* (2001), robustness is demonstrated classically by having large gain and phase margins in the closed-loop response. Furthermore, if a full loop transfer recovery is achieved, the full-state feedback LQ regulator performance will have a robustness of  $\pm 60^\circ$  phase margin and 6 db to infinite gain margin. Since our system is non-minimal phased, only partial recovery is expected. Since large gain and phase margins were obtained for the linear system, the performance of the LQG controller in terms of robustness should not be expected to be significantly different from that of the  $H_\infty$  controller.

In figure 1, we show the three-dimensional nonlinear plant model. The control input and measurement output of the model are Fourier–Chebyshev coefficients rather than their collocation point values. On the other hand, in the physical plant (such as in laboratory experiments) the input and output are physical temperature distributions. Since the LQG controller is formulated in the modal space, when the upper block represents the plant instead of the model, an FFT and an IFFT have to be performed, respectively, at the input and output of the controller. In our case, the LQG controller takes the measurements from the three-dimensional nonlinear plant model (Fourier coefficients at sensor planes) as input and determines a control action (Fourier coefficients at actuator plane) as output. The estimate state vector represents the vertical structure and the state matrices  $\mathbf{A}^*$ ,  $\mathbf{B}^*$ ,  $\mathbf{C}^*$  and  $\mathbf{D}^*$  are computed in terms of the designed values of wavenumber and Rayleigh number,  $\alpha_{km}^*$  and  $Ra^*$  (see equation (3.7) of Or *et al.* 2001).

The truncation numbers ( $K = 32, M = 32, N = 32 + 1$ ) considered here are of moderate size. It is still convenient to compute and pre-store the steady-state Kalman gain  $\mathbf{K}_f$  and regulator gain,  $\mathbf{K}_c$ . However, it is not feasible to pre-store the state matrices  $\mathbf{A}^*$  for all the wavenumbers. Instead, we compute  $\mathbf{A}^*$  for each set of wavenumbers at each time step in the time loop. At each time step, the three sensor plane temperatures, in modal coefficients,  $\theta_{km,s}(z_i, t)$  ( $i = 1, 2$  and  $3$ ) (see (2.8)), are exported from the nonlinear plant model. There are  $6(K + 1)M$  of such coefficients, corresponding to wavenumbers  $0$  to  $K\alpha_x$  in the  $x$  dependence and  $(-M + 1)\alpha_y$  to  $M\alpha_y$  in the  $y$  dependence. These values are then fed into the controller which consists of the Kalman filter and the regulator. The controller processes the information based on the measured data and determines the control output in terms of a set of  $2(K + 1)M$  modal coefficients for  $\theta_{km,c}(0, t)$ . These values are then input into the nonlinear model through the lower-wall boundary condition.

#### 2.4. Green's function for point sensors and actuators

In some experimental implementations (Tang & Bau 1998a), the sensors and actuators are discrete rather than continuous. For the low-resolution point sensors and actuators (typically with spacing between array points of  $O(d)$ ), it is desirable to stack the arrays of sensor and actuator points vertically on top of each other. Indeed, our result will show that the maximal effect of actuation caused by an impulse on the sensor plane occurs as a point collocated horizontally with the impulse. For a linear system, the controller input-to-output relationship can be expressed in the following integral form,

$$\theta_c(x, y, t) = \iint \iint G(x, y, t | x', y', t') \theta_s(x', y', t') dx' dy' dt', \quad (2.22)$$

where  $\theta_c(x, y, t)$  and  $\theta_s(x', y', t')$  are, respectively, the planar actuator and sensor temperature fields. Here,  $(x, y)$  and  $(x', y')$  denote coordinates for the actuator and sensor planes, respectively. The kernel  $G(x, y, t, |x', y', t')$  is a Green's function (or an influence function). The first three arguments in  $G$  represent the effect and the last three represent the cause.

In principle, the input and output of the LQG controller can be represented by a linear differential operator  $L$ . The precise form of  $L$  need not be specified here, since for our purpose the Green's function will be computed spectrally. In terms of  $L$ , we can describe some general properties of Green's function. The input and output temperatures to the controller are governed by  $L\theta_c = \theta_s$ , subject to appropriate lateral boundary conditions in  $x, y$ . The Green's formula for any two arbitrary functions  $u(x, y, t)$  and  $v(x, y, t)$  can be written as the sum of an integral  $\iint \iint (uLv - vL^+u) dx' dy' dt'$  and a number of terms evaluated at the lateral boundaries  $x = 0, 2\pi/\alpha_x$  and  $y = 0, 2\pi/\alpha_y$ . In the formula,  $L^+$  is the adjoint operator of  $L$ . Now if further restrictions are imposed on  $u$  and  $v$ , the Green's formula produces some important property about the Green's function. Let  $u = G(x, y, t | x_1, y_1, t')$  and  $v = G^+(x, y, t | x_2, y_2, t')$  where  $G$  and  $G^+$  satisfy, respectively,

$$\left. \begin{aligned} LG(x, y, t | x_1, y_1, t') &= \delta(x - x_1)\delta(y - y_1)\delta(t - t'), \\ L^+G^+(x, y, t | x_2, y_2, t') &= \delta(x - x_2)\delta(y - y_2)\delta(t - t'). \end{aligned} \right\} \quad (2.23)$$

In addition,  $G$  and  $G^+$  satisfy the appropriate lateral boundary conditions and adjoint boundary conditions so that the boundary terms in the Green's formula vanish. The



Green’s formula becomes

$$\int \int \int (G^+LG - GL^+G^+) dx' dy' dt' \equiv 0. \tag{2.24}$$

Substituting (2.23) into (2.24), we obtain Maxwell’s reciprocity relationship  $G(x_2, y_2, t|x_1, y_1, t') = G^+(x_1, y_1, t|x_2, y_2, t')$ . In our problem, the lateral boundary conditions are periodic. The differential operators in  $x$  and  $y$  are even in  $\partial_x$  and  $\partial_y$ . The linear operator  $L$  is self-adjoint, i.e.  $L \equiv L^+$  and the symmetric relationship holds,

$$G(x_2, y_2, t|x_1, y_1, t') = G(x_1, y_1, t|x_2, y_2, t'). \tag{2.25}$$

The symmetry relationship above can be interpreted as follows: at a given time  $t > t'$ , an actuator output of the controller at  $(x_2, y_2)$  due to a unit impulsive sensor input of the controller at  $(x_1, y_1)$  and time  $t'$  is equal to the actuator output at  $(x_1, y_1)$  due to a unit impulse sensor input at  $(x_2, y_2)$  and time  $t'$ .

Of particular interest here is the shape of the actuator temperature  $\theta_c(x, y, t)$  generated by a unit impulse temperature at a sensor point  $(x_p, y_p)$ , say, at  $t = t_p$ . The spatial roll-off of the actuator temperature affects the spatial resolution of the spacing between sensor points. Let the impulsive measurement be

$$\theta_s(x', y', t') = \delta(x' - x_p)\delta(y' - y_p)\delta(t' - t_p), \tag{2.26}$$

from (2.22) we obtain the Green’s function

$$\theta_c(x, y, t) = G(x, y, t|x_p, y_p, t_p). \tag{2.27}$$

For each Fourier mode that corresponds to the wave vector  $(k\alpha_x, m\alpha_y)$  (where  $-K/2 \leq k \leq K/2$  and  $-M/2 \leq m \leq M/2$ ), the coefficient represents an entry of measurement vector  $z$  in the filter equation, (2.21). We then have

$$u(z, k\alpha_x, m\alpha_y, t) = \int_0^t \exp(\mathbf{A}^* - \mathbf{K}_f \mathbf{C}^*)(t - \tau)z(\tau) d\tau. \tag{2.28}$$

Note that the homogeneous solution due to the initial condition decays rapidly and does not contribute for sufficiently large  $t$ . After the  $z$  and  $u$  of all the Fourier modes are computed, a FFT will transform the two sets of coefficients to  $\theta_s(x, y, z_s, t)$  and  $\theta_c(x, y, 0, t)$ , respectively. When  $\theta_s(x, y, z_s, t)$  is impulsive according to (2.26), then (2.28) gives the Green’s function.

### 3. Numerical results

#### 3.1. Nonlinear convection

Above the value  $Ra = Ra_{c0} \approx 1707.76$ , the no-motion state gives rise to steady two-dimensional convection rolls. Depending on the value of  $Pr$ , these rolls in turn will become unstable at still higher values of  $Ra$ , making transitions to two-dimensional oscillatory convection or steady three-dimensional convection depending on the value of the Prandtl number. Cross & Hohenberg (1993) give considerable detail about the bifurcation diagram.

Before engaging in the closed-loop numerical simulations, it is worth performing some comparisons to known results, as check cases for validating the nonlinear plant model. In Clever & Busse (1974), selective Nusselt number values for the two-dimensional convection solution were published. Table 1 shows the values of the Nusselt number,  $Nu$ , for several different values of  $Ra$  at  $Pr = 0.71$  and  $7.0$  for

---

$Ra$	$Pr = 0.71$	$Pr = 7.0$
2000	1.210 (1.212)	1.214 (1.214)
2500	1.472 (1.475)	1.475 (1.475)
10000	2.653 (2.661)	2.608 (2.618)

---

TABLE 1. Nusselt number values for two-dimensional rolls.

two-dimensional rolls at  $\alpha_x = 3.117$  ( $\alpha_y = 0$ ). The Nusselt number is a measure of the convective heat transfer, defined as the value of temperature gradient at either upper or lower wall,

$$Nu = 1 + \sum_{n=0}^N \theta_{00n} \left. \frac{dT_n(z)}{dz} \right|_{z=0,1}, \quad (3.1)$$

where the first two zero indices of  $\theta_{00n}$  correspond to  $k = m = 0$  so that the sum represents the temperature gradient averaged over the horizontal plane. In the absence of an internal heat source, the values of  $Nu$  evaluated at  $z = 0$  and  $z = 1$  should be equal. Our open-loop, steady-state solutions are obtained at truncation numbers  $K = 16$ ,  $M = 8$  and  $N = 16$ , for  $\alpha_x = 3.117$  and  $\alpha_y = 0$  (transverse rolls). In table 1, the values published in Clever & Busse (1974) are shown in parentheses. In all cases, the difference between our value and theirs is less than 0.4%. For values of wavenumber  $\alpha_x = 2.2$  and 2.6, respectively, where  $Pr = 7$  and  $Ra = 10000$ , we obtain  $Nu = 2.465$  and 2.548 versus their values 2.473 and 2.557. We further note that  $Nu$  should not depend on the orientation of rolls. As a consistency check, we compare the  $Nu$  of our solutions between the longitudinal ( $\alpha_x = 0$ ,  $\alpha_y \neq 0$ ) and transverse rolls ( $\alpha_x \neq 0$ ,  $\alpha_y = 0$ ). The difference of the  $Nu$  values is found to be less than 0.02%.

### 3.2. Proportional feedback control

We now turn to the proportional feedback control problem. From the results of Tang & Bau (1994) and Or *et al.* (2001), oscillatory convection occurs when the proportional gain  $K_p$  becomes sufficiently large. At  $K_p = 6$ , for instance, the linear theory at  $Pr = 7$  predicts that an oscillatory instability is preferred over the steady-state rolls. The closed-loop threshold of stability is  $\alpha_c = 3.73$  and  $Ra = 3.63Ra_{c0}$ , with the frequency of oscillation equal to 20.4. For the same values of  $Ra$  and wavenumber we use the steady state two-dimensional rolls as the initial conditions for our time-domain simulation. Our results appear to be consistent with the prediction of linear theory. Figure 2 shows the behaviour of  $Nu$  of the closed-loop solutions at  $K_p = 6$  for two values of  $Ra/Ra_{c0}$ : at 3.55 (solid) and 3.65 (dashed). In both curves, the open-loop steady two-dimensional rolls are used as the initial condition. These rolls are obtained at  $Ra/Ra_{c0} = 3.65$  and  $\alpha_x = 3.73$  which yield  $Nu = 2.273$ . In figure 2 the solid curve shows stable behaviour whereas the dashed curve is unstable. The neutral curve has  $Ra/Ra_{c0}$  approximately equal to 3.60. This value is in close agreement with the result of linear theory. Furthermore, the oscillatory behaviour in the curves indicate a frequency of about 40.3, again consistent with eigenvalue prediction of  $2 \times 20.4$  of the linear theory. It is noted that  $Nu$  has a harmonic frequency equal to twice the fundamental frequency.

The oscillatory convection appears to have a two-dimensional roll planform. The more interesting finding according to the numerical simulations is that this oscillatory solution is not unique for the given set of external parameters. It turns out when we prescribe an additional small perturbation field in the  $y$ -dependence, for the same

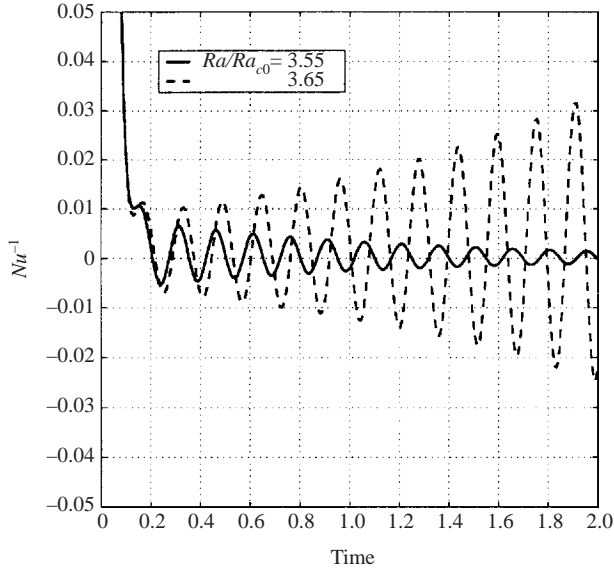


FIGURE 2. Nusselt number of oscillatory convection.

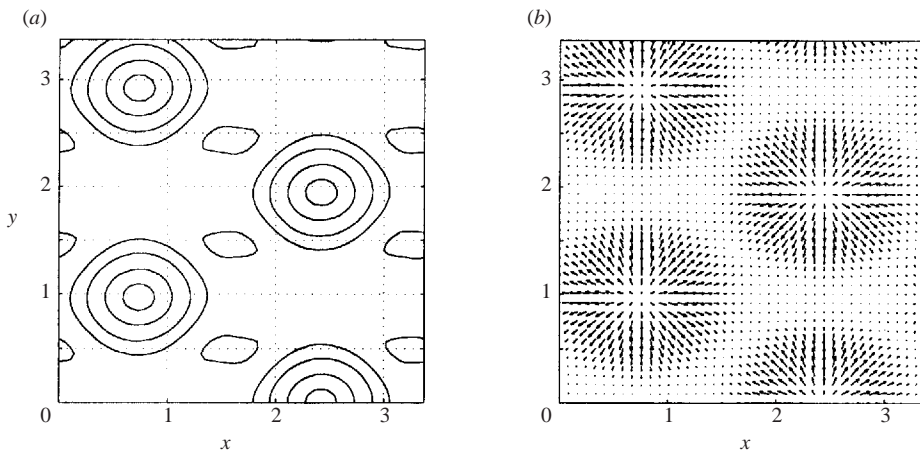


FIGURE 3. Closed-loop solution: g-type hexagon pattern.

values of  $K_p$ ,  $Ra$  and  $\alpha_x$ , the closed-form solution will not settle at the two-dimensional oscillatory branch if the cross-roll perturbation is not small. For sufficiently large cross-roll perturbations, the solution will settle down at a subcritical branch. In this case, the horizontal planform solution is three-dimensional, which resembles the g-type hexagons (Or & Kelly 2001). Depending on the asymmetry in the perturbation temperature, hexagon cells with sinking motion near the centre of the cell and rising motion near the cell wall is referred to as the g-type. For the  $\ell$ -type hexagons the opposite is true. In figure 3, we show (a) the planform corresponding to temperature at the lower wall ( $z = 0$ ) and (b) the planform corresponding to horizontal velocity components at horizontal plane  $z = 0.1$  (the velocity components vanish at the lower wall owing to a non-slip boundary condition). The three-dimensional hexagonal convection is a steady-state pattern and corresponds to  $Nu = 1.4352$ . The hexagonal

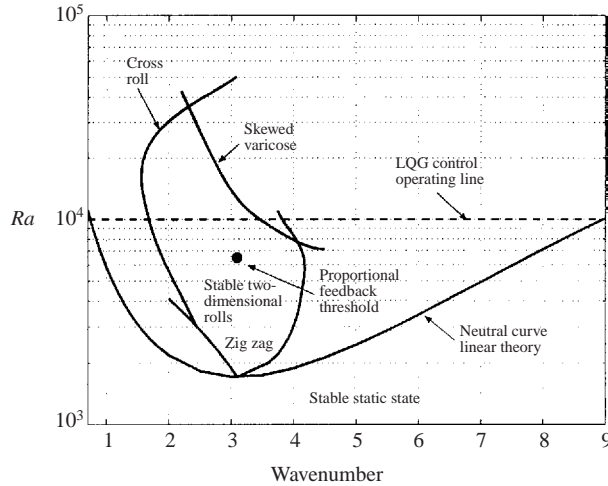


FIGURE 4. A sketch of the stability boundaries for the uncontrolled layer at  $Pr = 7.0$ .

solution induced by the controller action has been studied in considerable detail (see Shortis & Hall 1996; Or & Kelly 2001) based on weakly nonlinear analysis. Here, we actually obtain the solution from a direct numerical simulation. We summarize several important conclusions based on the results presented. (i) The solutions obtained from our fully nonlinear three-dimensional pseudospectral plant model have been checked and agree reasonably well against known published results from other independent methods. (ii) The proportional feedback controller induces a subcritical range of  $g$ -type hexagonal convection, which appears to be captured in the nonlinear simulations. Near the stability threshold of the closed-loop system with sufficiently large gain, both two-dimensional oscillatory convection and three-dimensional steady-state hexagonal convection can co-exist in the same parameter region. Next, we consider the closed-loop simulation using the LQG controller.

### 3.3. Closed-loop simulations using the LQG controller

We investigate the closed-loop system with an operating condition of the plant model at  $Pr = 7.0$  and  $Ra = 10^4$ . In the set-up, the controller gains  $\mathbf{K}_f$  and  $\mathbf{K}_c$  are steady states, precomputed and stored. The actual controller and the nonlinear plant models are implemented in *FORTTRAN* and *MATLAB*. This controller is implemented according to the description in §2.3.

In figure 4, we provide a sketch of the stability diagram of the uncontrolled dynamics at  $Pr = 7$  (see Busse & Clever 1979, figure 1 for the original plot). The stability boundary of the purely conduction (static) state is the lowest parabolic-shaped curve. At each  $Ra$  above the minimum of this neutral curve (supercritical), the linear theory predicts an outer band of wavenumbers in which the basic state is unstable. However, at each supercritical  $Ra$ , the stable finite-amplitude convection occurs in a narrower band of wavenumbers. At  $Pr = 7$ , the stable finite-amplitude convection in the inner band corresponds to steady two-dimensional convection rolls. For  $Ra = 10^4$  (the dashed line in figure 4), the inner band of wavenumbers is bounded on the lower side by the cross-roll instability at  $\alpha \approx 1.75$  and on the higher side by the skew-varicose instability at  $\alpha \approx 3.5$ . At this  $Ra$ , the inner band of wavenumbers is significantly smaller than the outer band obtained from the linear theory, which

gives approximately 0.74 and 9.0, respectively. The stability boundaries are in general  $Pr$  dependent.

The stable two-dimensional convection rolls are characterized by a single wavenumber, but it can be any value within the inner band. Laboratory experiments (see Cross & Hohenberg 1993) using different initial conditions had demonstrated that the stable pattern can have a non-unique wavenumber. On the other hand, certain experiments performed by letting  $Ra$  vary either as a slow function of time or by inducing a spatial ramp in the layer thickness indicate that the rolls are realized with a unique wavenumber. Since our goal here is to eliminate the convection pattern, the detailed properties of the nonlinear solution do not concern us other than as the initial condition for our closed-loop solutions.

The closed-loop simulation is demanding computationally in the sense that the entire outer band of wavenumbers should be covered in the stabilization of the basic state. In our simulation, the fundamental wavenumbers  $\alpha_x$  and  $\alpha_y$  are selected so that the expansion covers the entire inner band, but falls short of the outer band. We argue that this arrangement is reasonable and we use the truncation numbers  $K = M = N = 32$ . The nonlinearity has the role of limiting the wavenumber of the convection pattern to the inner band. As the initial condition for the closed-loop simulation, we let  $\alpha_x = 1.0$  in the open-loop run with appropriate initial condition. We obtain a steady, two-dimensional roll pattern with a wavenumber of 3.0. In the closed-loop simulation, we add in a small perturbation of cross-rolls superimposed on the steady finite-amplitude rolls. The added perturbation assures that the initial condition used is three-dimensional.

The closed-loop simulation results are shown in figures 5(a)–5(g). Since the transition is two-dimensional, it suffices to reveal the flow fields by showing the cross-sectional view in the  $(z, x)$ -plane. In figures 5(a)–5(c), we show the transient pattern of the perturbation isotherms in the  $(x, z)$ -plane (with basic temperature subtracted). The three isotherm patterns (figures 5a–5c) of the disturbance field are snapshots obtained at  $t = 0, 0.05$  and  $0.2$  diffusive time units, respectively. Note that the upper and lower wall are both the perturbation isotherm of zero temperature. The solid (dashed) lines indicate positive (negative) increments of temperature. The same increment of temperature applies to all three panels. Figure 5(a) shows the cross-section of the steady-state convection rolls used as the initial condition at  $t = 0$ . Shortly after the controller is turned on at  $t = 0$ , figure 5(b) shows that a steep thermal boundary-layer pattern develops near the lower wall at  $t = 0.05$ . This boundary temperature perturbation possesses an opposite sign to the perturbation in the bulk of the layer of fluid, and therefore exerts a cancellation effect, which tends to drive the fluid towards an isothermal state. Figure 5(c) shows at a later instant ( $t = 0.2$ ) that the isotherm pattern indeed settles towards a static state. Here, the isotherms correspond to a residual temperature distribution of about 1.5% of the temperature shown in figure 5(a). The residual temperature continues to approach zero asymptotically in time.

In figures 5(d)–5(f) we show the quiver plots of the velocity field corresponding to isotherms in figures 5(a)–5(c). The arrow sizes in figures 5(e)–5(f) are according to the true relative scale. For illustration of the flow field we deliberately magnify the arrows in figure 5(f). Note that the velocity rolls are shifted by a phase of  $\pi/2$  relative to the isotherm rolls. The upward (downward) motion of fluid is associated with the positive (negative) isotherms, as indicated in the figures. From figure 5(e), we observe that the upwelling and downwelling regions are significantly perturbed by the control action. As a result, a secondary row of vortices near the lower wall

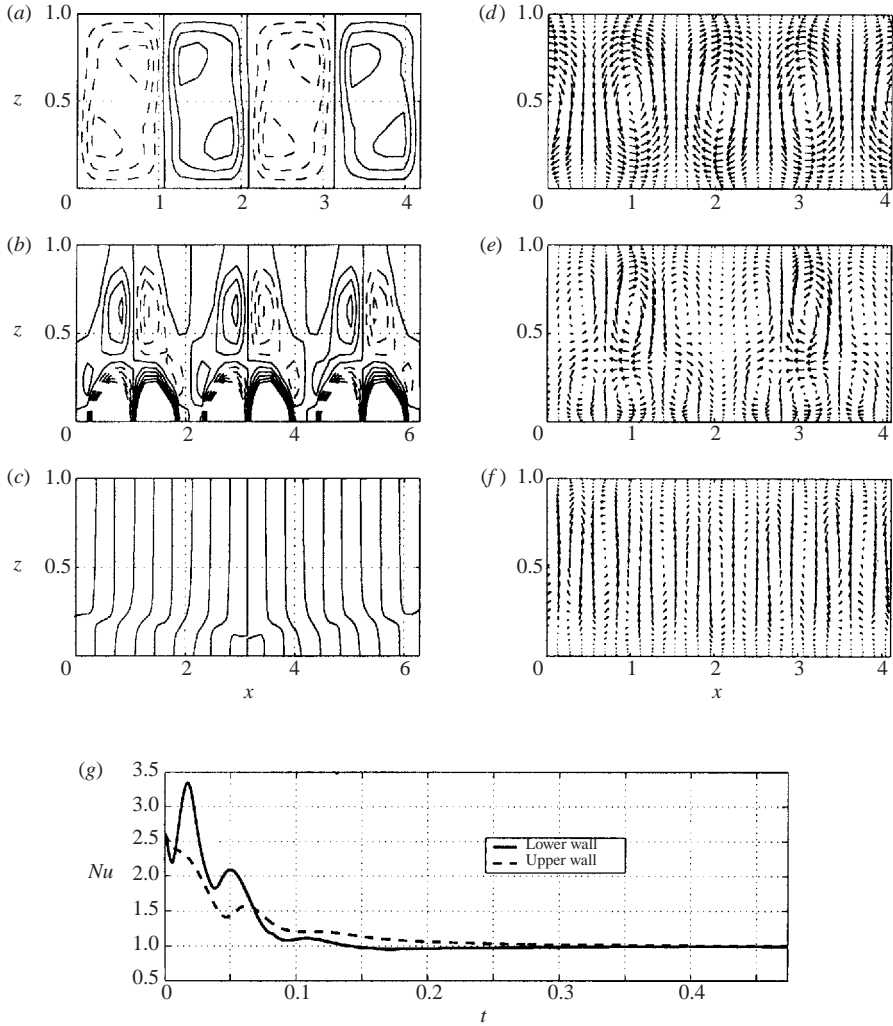


FIGURE 5. (a)–(c) Transient patterns of isotherm under controller action; (d)–(f) corresponding velocity quivers of the flow patterns; (g) Time response of Nusselt numbers at the lower and upper wall ( $Ra = 10^4$  and  $Pr = 7.0$ ) (a), (d)  $t = 0$ ; (b), (e) 0.05; (c), (f) 0.2.

is apparent. In figure 5(e), the convective motion becomes so weak that the vortex structure is no longer visible. Finally, we show the two Nusselt numbers in figure 5(g) in time as the indicator for convective heat transport. The lower (solid) and upper (dashed) curves are based on the horizontal-mean temperature gradient at the lower and upper walls, respectively. The gradient is computed normal to the walls. As the thermal actuator action is switched on, a large transient perturbation develops near the lower wall, indicating an increase in local heat flux from the actuator action. The lower Nusselt number shoots up considerably higher than the upper Nusselt number initially for a brief duration. Subsequently, the upper Nusselt number is greater than the lower value, as the heat in the bulk of fluid is transferred away. Between  $t = 0$  and  $t = 0.474$ , we determined through integration that the areas under the curves are 0.5635 (solid line) and 0.5628 (dashed line). The two integral values will converge to the same value in time, as a constraint of the conservation of heat.

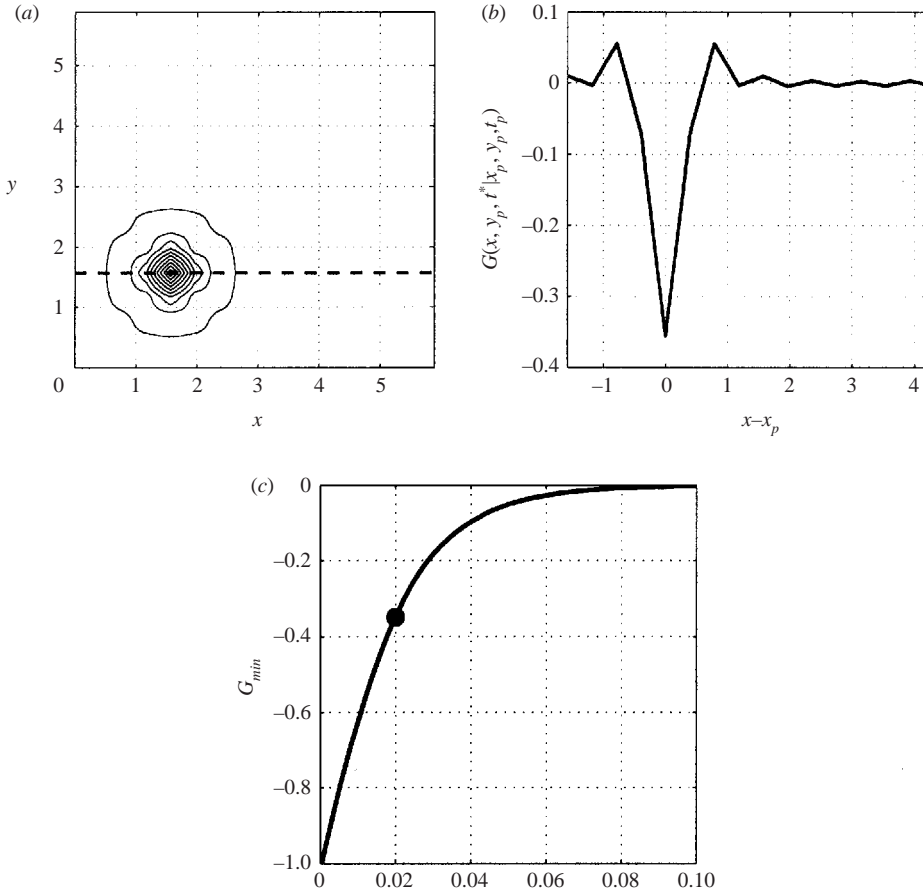


FIGURE 6. (a) Isotherms of the response of temperature on the actuator plane owing to an impulse source temperature on the sensor plane; (b) variation of the response temperature along the dashed line of (a); (c) change of  $G_{min}$  with  $t^*$ .

For a related drag reduction control problem, Cortelezzi & Speyer (1998) developed a robust reduced-order controller. It is beyond the present scope to consider a reduced-order controller for this nonlinear simulation. Here, on the other hand we determine the spatial roll-off characteristic of the controller based on the Green's function approach. The roll-off characteristics will shed light on the spatial resolution of the arrays of discrete sensors and actuators required for a successful control. A good spatial roll-off implies that relatively few measured points are required to achieve an effective control (see Bamieh & Dahleh 2001). We refer to the description in §2.4. Consider the same case in the numerical simulation for  $Pr = 7$  and  $Ra = 10^4$  and a length scale of the layer corresponding to  $\alpha_x = 1$  and  $\alpha_y = 1$ . Figure 6(a) shows the contour of the Green's function  $G(x, y, t^* | x_p, y_p, t_p)$ , which is the response temperature on the actuator plane  $z = 0$  owing to an impulse temperature  $\delta(x - x_p)\delta(y - y_p)\delta(t - t_p)$  on the sensor plane  $z_s = 0.3$ . Here, we let  $x_p = 1.5$ ,  $y_p = 1.5$  and  $t_p = 0$ ,  $t^* = 20\Delta t$  with  $\Delta t = 10^{-3}$ . Figure 6(b) shows the response temperature profile as a function of  $x - x_p$  along the dashed line designated in figure 6(a). The response temperature corresponds to  $G(x, y_p, t^* | x_p, y_p, t_p)$  (with  $t^* > t_p$ ). The result shows that the function has a negative minimum, here denoted by  $G_{min}$ . The minimum is collocated horizontally

with the sensor impulse. The negative temperature generated is intended to cancel the disturbance temperature created by the impulsive temperature. Of particular significance is how steep the response curve (in V-shaped) is, implying that the influence zone about the sensor point is small. From figure 6(b), the base width of the V-shape curve is about the width of one roll, assuming that the length scale of the roll does not differ significantly from its critical value. In order for the controller to stabilize the convective disturbance, the spacing between successive points in the array cannot be greater than the effective width of the response temperature.

The plots in figure 6(a)–6(b) represent a snapshot at  $t = t^*$ . We observed that as  $t^*$  increases from 0, the shape and width of the temperature profile (see figure 6b) have changed little, but the magnitude of the minimum decreases rapidly. In figure 6(c), we show the change of the temperature at the minimum,  $G_{min}$ , with  $t^*$ . The large dot in figure 6(c) denotes the point corresponding to the snapshot of figures 6(a)–6(b). Since the system is diffusive, the response temperature decays monotonically in time, as expected.

#### 4. Experimental considerations

For implementation of the LQG feedback control design, an experiment of RBC is considered. This effort will be guided by the result of the nonlinear simulation, modified for air at room temperature (with  $Pr \approx 0.7$ ) as the working fluid. Although the closed-loop numerical results presented earlier in the paper is for the case  $Pr = 7.0$  only, our supplementary analysis completed only recently at  $Pr = 0.71$  has revealed that there is no significant difference in the closed-loop response between the two Prandtl numbers for the condition  $Ra = 10^4$ .

For RBC, previous experiments demonstrate that the initial and onset conditions, as well as the realized convection pattern, are predictable under controlled experimental conditions (Cross & Hohenberg 1993). Complex situations in applications such as variations of material properties, occurrence of concentration gradient and solutal convection, presence of horizontal basic temperature gradient, sidewall effects, defects in pattern, etc., are not included.

In the experimental apparatus, the upper and lower walls will be of two types of material with a large range of heat conductivity. The two walls have large aspect ratio to the layer depth, and may have different thermal boundary conditions. Miniature strain gauge type heaters will be strategically placed at the lower wall as actuator (with separation between heaters determined by the wavelength of the pattern to be controlled). For air, it is convenient to use the holographic interferometry as the sensing technique. Such a sensor can detect temperature differential to high precision. Our LQG controller design has been validated using simulated sensor data. Eventually, for implementation in the experiment, a reduced-order LQG controller will be developed. The three-dimensional pseudospectral model will be modified to accommodate the spatial and temporal dynamics of the sensors and actuators, guided by laboratory observations and the experimental data.

#### 5. Conclusion

The goal achieved in this study is a successful demonstration through numerical simulations that a fully nonlinear steady and preferred state of convection in a horizontal layer of fluid can be reverted to the no-motion state by closed-loop controller action. The simulated results here show the performance of the LQG



controller at  $Ra = 10^4$  and  $Pr = 7$ . At this  $Ra$ , the proportional feedback controller is ineffective according to the linear theory. For even higher values of  $Ra$ , stabilization is likely to be achievable with the LQG controller by using higher spatial resolution in the simulation, but we have not pushed for that result. The reason is that for realistic modelling at high  $Ra$  the effects of the discrete actuator and actuator delay are important considerations as well. Although a general stability proof cannot be inferred from the nonlinear simulation of a few initial conditions, the results do indicate that the linear controller appears quite responsive in suppressing important finite disturbances.

The numerical method used here to develop the nonlinear plant model is pseudospectral spatially. The integration of the model dynamics equation is performed by a time-splitting technique. We have adopted the conventional scheme developed in Marcus (1984) (also see Canuto *et al.* 1986). However, since some significant modification of the scheme has been made, we validate our fully nonlinear three-dimensional plant model by comparing check cases against published results, in particular, from Clever & Busse (1974) and Busse & Clever (1979). The agreement appears reasonably good. Moreover, the direct simulation verifies the results of the weakly nonlinear analysis (Or & Kelly 2001) about the presence of the controlled-induced subcritical g-hexagon solution.

We have also examined the shape function of the actuator response by computing the Green's function of the LQG controller. The shape of the actuation temperature determines the order of the horizontal distance between points of the sensor/actuator arrays in term of the layer gap thickness  $d$ . This information is of critical importance when the more realistic pointwise sensor and actuator are used instead of the continuous ones.

This research is supported by the United States Air Force (Grant no. F49620-00-1-0166).

#### REFERENCES

- BAMIEH, B. & DAHLEH, M. 2001 Energy amplification in channel flows with stochastic excitation. *Phys. Fluids* **13**, 3258–3269.
- BODENSCHATZ, E., PESCH, W. & AHLERS, G. 2000 New developments in Rayleigh–Bénard Convection. *Annu. Rev. Fluid Mech.* 709–778.
- BUSSE, F. H. & CLEVER, R. M. 1979 Instabilities of convection rolls in a fluid of moderate Prandtl number. *J. Fluid Mech.* **91**, 319–335.
- CANUTO, C., HUSSAINI, N. Y., QUARTERONI, A. & ZANG, T. A. 1986 *Spectral Methods in Fluid Dynamics*. Springer.
- CLEVER, R. M. & BUSSE, F. H. 1974 Transition to time-dependent convection. *J. Fluid Mech.* **65**, 625–645.
- CORTELEZZI, L. & SPEYER, J. L. 1998 Robust reduced-order controller of laminar boundary layer transition. *Phys. Rev. E* **58**, 1906–1910.
- CROSS, M. C. & HOHENBERG, P. C. 1993 Pattern formation outside of equilibrium. *Rev. Mod. Phys.* **65**, no. 3, part 2.
- GOTTLIEB, D. & ORSZAG, S. A. 1977 *Numerical Analysis of Spectral Methods: Theory and Applications*. SIAM-CBMS, Philadelphia.
- HOWLE, L. E. 1996 A comparison of the reduced Galerkin and pseudospectral methods for simulation of steady Rayleigh–Bénard convection. *Intl J. Heat Mass Transfer* **39**, 2401–2407.
- HOWLE, L. E. 1997a Linear stability analysis of controlled Rayleigh–Bénard convection using shadowgraphic measurement. *Phys. Fluids* **9**, 3111–3113.
- HOWLE, L. E. 1997b Control of Rayleigh–Bénard convection in a small aspect ratio container. *Intl J. Heat Mass Transfer* **40**, 817–822.

- HOWLE, L. E. 1997*c* Active control of Rayleigh–Bénard convection. *Phys. Fluids* **9**, 1861–1863.
- HOWLE, L. E. 2000 The effect of boundary properties on controlled Rayleigh–Bénard convection. *J. Fluid Mech.* **411**, 39–58.
- MARCUS, P. S. 1984 Simulation of Taylor–Couette flow. Part 1. Numerical methods and comparison with experiment. *J. Fluid Mech.* **146**, 45–64.
- OR, A. C., CORTELEZZI, L. & SPEYER, J. L. 2001 Robust feedback control of Rayleigh–Bénard convection. *J. Fluid Mech.* **437**, 175–202.
- OR, A. C. & KELLY, R. E. 2001 Feedback control of weakly nonlinear Rayleigh–Bénard–Marangoni convection. *J. Fluid Mech.* **440**, 27–47.
- PRESS, W. H., TEUKOLSKY, S. A., VETTERLING, W. T. & FLANNERY, B. P. 1992 *Numerical Recipes. The Art of Scientific Computing*, 2nd edn. Cambridge University Press.
- RHEE, I. & SPEYER, J. L. 1991 A game theoretic approach to a finite-time disturbance attenuation problem. *IEEE Trans. Automat. Contr.* **36**, 1021–1032.
- SHORTIS, T. A. & HALL, P. 1996 On the effect of feedback control on Bénard convection in a Boussinesq fluid. *NASA Contractor Rep.* 198280: ICASE Rep. 96-9.
- TANG, J. & BAU, H. H. 1993 Stabilization of the no-motion state in Rayleigh–Bénard convection through the use of feedback control. *Phys. Rev. Lett.* **70**, 1795–1798.
- TANG, J. & BAU, H. H. 1994 Stabilization of the no-motion state in the Rayleigh–Bénard problem. *Proc. R. Soc. Lond. A* **447**, 587–607.
- TANG, J. & BAU, H. H. 1998*a* Experiments on the stabilization of the no-motion state of a fluid layer heated from below and cooled from above. *J. Fluid Mech.* **363**, 153–171.
- TANG, J. & BAU, H. H. 1998*b* Numerical investigation of the stabilization of the no-motion state of a fluid layer heated from below and cooled from above. *Phys. Fluids* **10**, 1597–1610.